

Synergistic modulation of ionic selectivity in graphene pores modified by crown ether

Yanbo Xin(辛延波), Qin Gao(高勤), Jiangshun Huang(黄江顺), Paul K. Chu(朱剑豪), and Anping Huang(黄安平)
Citation: Chin. Phys. B, 2026, 35 (**8**): 086102. DOI: 10.1088/1674-1056/ae5c74
http://cpb.iphy.ac.cn; http://iopscience.iop.org/cpb

What follows is a list of articles you may be interested in

A novel stack-HfO_2 top-gate structure for improving performance of network carbon nanotube transistor

Bowen Zhang(张博文), Yimin Lei(雷毅敏), Jiejie Zhu(祝杰杰), Weiwei Wang(王巍巍), Yuxiang Wei(魏宇翔), Lingjie Qin(秦灵洁), Mingchen Zhang(张明辰), Jiaxiang Xu(徐佳响), Hong Wang(王宏), Xiaohua Ma(马晓华), and Yue Hao(郝跃)
Chin. Phys. B, 2026, 35 (**5**): 056103. DOI: 10.1088/1674-1056/ae067e

Improved temperature localization by hollowing plasmonic nanofocusing cones

Jiaming Zhang(张家明) and Jinglai Duan(段敬来)
Chin. Phys. B, 2025, 34 (**6**): 066104. DOI: 10.1088/1674-1056/adc409

Effect of copper/tungsten heterophase interface on radiation resistance: Insights from atomistic simulations

Wen Chen(陈文), Min Li(李敏), Bao-Qin Fu(付宝勤), Tun Chen(陈暾), Jie-Chao Cui(崔节超), and Qing Hou(侯氢)
Chin. Phys. B, 2025, 34 (**4**): 046108. DOI: 10.1088/1674-1056/adb40d

Design and preparation of amorphous carbon nanotubes reinforced copper

Xiaona Ren(任晓娜), Wentao Wu(吴文涛), Zhipei Chen(陈志培), and Changchun Ge(葛昌纯)
Chin. Phys. B, 2025, 34 (**4**): 046107. DOI: 10.1088/1674-1056/adb8b7

Magnetostatic interaction in electrodeposited Ni/Au multilayer nanowire arrays

Li-Zhong He(何丽忠), Li-Rong Qin(秦丽溶), Jian-Wei Zhao(赵建伟), Ying-Ying Yin(殷营营), Yu Yang(杨瑜), Guo-Qing Li(李国庆)
Chin. Phys. B, 2016, 25 (**8**): 086101. DOI: 10.1088/1674-1056/25/8/086101

Synergistic modulation of ionic selectivity in graphene pores modified by crown ether

Yanbo Xin(辛延波)[1], Qin Gao(高勤)[3], Jiangshun Huang(黄江顺)[2], Paul K. Chu(朱剑豪)[4], and Anping Huang(黄安平)[2,†]

[1] *Department of Fundamental Courses, Shanxi Institute of Technology, Yangquan* 045000, *China*
[2] *School of Physics, Beihang University, Beijing* 100191, *China*
[3] *School of Applied Science, Beijing Information Science & Technology University, Beijing* 102202, *China*
[4] *Department of Physics, Department of Materials Science and Engineering, and Department of Biomedical Engineering, City University of Hong Kong, Tat Chee Avenue, Kowloon, Hong Kong, China*

(Received 7 January 2026; revised manuscript received 24 March 2026; accepted manuscript online 8 April 2026)

Achieving high ion selectivity in atomically thin membranes represents a critical step toward advanced gating-controlled ionic transport in nanofluidic applications such as logic gates and biosensors. Herein, monolayer graphene pores modified by crown ether are constructed to systematically investigate the ion selectivity in both vacuum and aqueous environments from a theoretical perspective. Synergistic optimization of charge distribution and pore size significantly improves the ion selectivity, showing a cation/anion selectivity ratio of up to 10^2. The energy profiles for ion penetration (e.g., Li^+, Na^+, K^+, Cl^-, Br^-) are modulated by tailoring the pore size and introducing charges, as validated by kinetic analysis of ion-free diffusion and electroosmotic flow. The fundamental ion-sieving mechanism is further elucidated by examining the dependence of ion currents on carrier concentration in the nanopores. These findings on ion transport pave the way for artificial nanochannel membrane applications in nanofluidic circuits and biomimetic sensors.

Keywords: graphene crown ether pores, charge selectivity, ion penetration, nanochannels

PACS: 61.46.–w, 82.39.Wj, 87.16.dp, 87.16.Vy

DOI: 10.1088/1674-1056/ae5c74 **CSTR:** 32038.14.CPB.ae5c74

1. Introduction

Charge selectivity, involving cations and anions, widely exists in artificial channels and membranes, and holds significant promise in advanced technologies such as logic gates and biosensors.[1–4] Two-dimensional (2D) materials, such as graphene with nanochannels, exhibit advantages in enhancing the ionic permeability efficiency due to their ultra-short ion transport pathways.[5–9] However, the charge-selective behavior diminishes at sub-nanometer thicknesses, necessitating functionalized nanochannels to achieve ion discrimination in ultrathin membranes.[10–12] In this respect, functionalization using crown ether is a powerful strategy for ion recognition,[13–15] enabling pioneering advances in nanofluidic systems, including stress-gated K^+ transport,[16] H^+ hopping mechanisms for fuel cell membranes,[17] enhanced Na^+ rejection in desalination,[16,17] and improved durability in Li–S batteries.[18] In fact, the graphene-crown ether architecture has recently established neuromorphic ionic responses (e.g., memcapacitance, K^+ delay) to expand the frontiers of bio-inspired iontronics.[14] These achievements leverage the size-matching specificity of crown ether (e.g., 18-crown-6/K^+, 15-crown-5/Na^+, 12-crown-4/Li^+),[15,17,19,20], where optimal steric binding ensures high-affinity cation capture at the ring center.[21,22] While such strong complexation is advantageous to selective recognition, it introduces an inherent energy barrier for cation translocation through confined pores. Consequently, efficient ion permeation in these systems often necessitates external stimuli (e.g., a bias voltage), and it is necessary to enhance the dynamic controllability of ion transport without compromising the selectivity.

Herein, we propose a strategic nanopore design via simulations of crown ether-functionalized graphene to achieve synergistic control of ion sieving and separation. The governing role of targeted structural adjustments on ion penetration profiles (first-principles calculations) and on cation selectivity in aqueous solutions (molecular dynamics simulations) is systematically investigated. Our results reveal exceptional cation selectivity in the engineered nanochannels, with cation-to-anion current flux ratios exceeding 10^2:1 and demonstrate programmable control of ion transport without external bias dependence. The results provide valuable insights into the design and fabrication of thin films with selective permeability of charges in nanoscale spaces.

2. Computational methods

2.1. First-principles calculation

The calculation was performed with the Vienna *Ab initio* Simulation Package[23] using the projector augmented wave

†Corresponding author. E-mail: aphuang@buaa.edu.cn

© 2026 Chinese Physical Society and IOP Publishing Ltd. All rights, including for text and data mining, AI training, and similar technologies, are reserved.

(PAW) potentials of Perdew–Burke–Ernzerhof (PBE).[24] Transition state search was performed by the climbing-image nudged elastic band (CI-NEB) method by VASP-VTST.[25] The optimized C–C bond length was 1.424 Å, in good agreement with the experimental data.[26] Multiple distinct defect types were engineered within the intrinsic graphene membrane. These comprised a series of carbon-deficient nanopores (14-carbon-4, ∼ 3.7 Å; 18-carbon-6, ∼ 5.7 Å; 24-carbon-9, ∼ 7.9 Å; 26-carbon-10, ∼ 8.6 Å), accompanied by crown-ether-like nanostructures of similar dimensions (e.g., 14-crown-4 ether) for comparisons, as shown in Fig. 1. The thermodynamic stability of the latter crown-ether-like structures was investigated using *ab initio* molecular dynamics (AIMD), as depicted in Fig. S1 of the supporting information. The Brillouin zone with a $3 \times 3 \times 1$ *k*-point mesh was sampled in all cases except structural optimization and transition state search and set to $1 \times 1 \times 1$. A plane wave cutoff energy of 550 eV was used in all cases. Meanwhile, the electron energies are converged to within a tolerance of 1×10^{-7} eV, and all the atoms were allowed to relax in the geometric optimization until the force on each atom is 1×10^{-2} eV/Å. Structure modeling and analysis were based on visualization by the electronic and structural analysis (VESTA) software.[27]

2.2. Molecular dynamics simulation

A computational model was adopted to investigate ionic currents through nanopores in a bilayer graphene array immersed in a 0.5-mol/L KCl solution. The model featured a 4×4 nanochannel grid, with each channel composed of paired nanopores. The force field and partial atomic charges were adopted from the benchmark study by Smolyanitsky *et al.* for graphene-embedded crown-ether pores: oxygen atoms in the crown ether ring were assigned a charge of $-0.4e$, and the adjacent carbon atoms were assigned positive charges to maintain overall charge neutrality of the system.[15] K^+ and Cl^- were selected for MD validation because they enable simultaneous resolution of steric and electrostatic effects within a single simulation, offering the most direct mechanistic validation — while KCl serves as a canonical experimental benchmark for broad comparability. The simulation commenced with an energy minimization step using the LAMMPS molecular dynamics software,[28] followed by equilibration in the NVT ensemble for 40 ns at a temperature of 300 K. Periodic boundary conditions were applied in all three dimensions (p p p). For the diffusion selectivity analysis (without applied electric field), the simulation box was capped at both ends in the *z*-direction by graphene nanosheets to confine the ions and water within two closed compartments. For the electroosmotic flow analysis, no such caps were applied, and an electric field was applied along the *z*-axis. Data from the full 40-ns trajectory were used for the diffusion selectivity analysis, while data from 2 ns to 40 ns were used for the electroosmotic flow analysis. This framework, facilitated by LAMMPS, offers insights into ion transport phenomena within graphene nanopores.

3. Results and discussion

3.1. Modulation of energy profiles

Ion penetration through graphene necessitates overcoming an energy barrier or traversing an energy potential well. Investigating the energy profiles associated with this penetration is crucial, as it elucidates the underlying transport mechanisms and the intricate interactions between ions and the graphene lattice. A comprehensive understanding of this process, including the analysis of the kinetics and fundamental mechanisms governing ion selectivity through graphene membranes, is essential for advancing applications based on graphene-based materials. This knowledge is paramount in order to discern the factors that dictate ion mobility and selectivity across such materials.

3.1.1. Pristine graphene

Pristine graphene, characterized by its tightly packed structure of single-layer six-membered carbon rings, poses a formidable barrier to ion penetration. This impermeability extends even to the smallest of atoms,[29–31] thereby rendering pristine graphene a highly impervious material on the atomic scale. To verify this experimental conclusion, ion nanochannels are constructed in a complete graphene membrane, and the permeation behavior of lithium (Li^+), sodium (Na^+), potassium (K^+), chlorine (Cl^-), and bromine (Br^-) ions is studied, as shown in Fig. 1(a). The potential energy zero is defined relative to the total energy of the system when the ion is 15 Å away from the graphene nanosheet, at which distance their interaction is negligible. This configuration serves as the reference point for analyzing the energy profiles associated with ion penetration through the graphene lattice. Climbing image nudged elastic band (CI-NEB) simulations[32] are applied to ascertain the transport pathway for lithium ions and to derive the energy profile associated with ion penetration through the graphene layer.

With this reference, the results indicate that the energy profiles for ion penetration through a pristine graphene layer are symmetric. Upon approaching the sheet, the ion adsorbs onto either face. Full penetration occurs only when the ion overcomes the central energy barrier and transfers to the opposite side. The findings reveal that the energy barriers for the penetration of Li^+, Na^+, K^+, Cl^-, and Br^- through a single-layer, intact graphene structure are high at 8.81 eV, 35.45 eV, 62.87 eV, 43.94 eV, and 63.66 eV, as shown in Fig. 1(a) and Table S1. The energy profile exhibits a symmetrical configuration, with the lowest energy points located on either side of the graphene, corresponding to the adsorption sites for ions

on the surface of the graphene. These energy barriers pose a challenge for ion permeation at room temperature, showing an average translational kinetic energy:

$$E = \frac{3kT}{2}, \tag{1}$$

where k is Boltzmann's constant and T is the temperature in Kelvin, rendering the barrier insurmountable under such conditions. The mechanism of ions permeating the pristine graphene structure is analyzed using the electron cloud density distribution. Carbon atoms are arranged in a hexagonal lattice through sp^2 hybridization in graphene, and valence electrons are distributed in a corresponding hexagonal lattice pattern. The larger atomic radius and the larger number of valence electrons in carbon atoms result in a denser electron cloud in the monolayer graphene. The increased density of the electron cloud hinders ion migration and decreases the ionic conductivity in graphene.

3.1.2. Defective graphene

Defects produced naturally during the synthesis and processing of graphene significantly influence the ion penetration behavior in the structure. Different types of defect structures, such as 14-carbon-4, 18-carbon-6, 24-carbon-9, and 26-carbon-10, are studied, as shown in Figs. 1(b) and 1(c). Graphene with atomic-scale defects[33,34] exhibits enlarged electron cloud "holes", as shown in the insets of Fig. 1(b), to regulate the ion penetration energy profiles. As shown in Figs. 1(b) and 1(c), when the pore size increases, the ion penetration energy potential barrier decreases and eventually vanishes. Among the ions tested, the energy profile for K^+ is dramatically altered: from presenting a substantial barrier of 62.87 eV in the pristine structure to featuring a pronounced adsorption well (−3.50 eV) in the 26-carbon-10 nanopore. Similarly, for Cl^-, the energy extremum changes from a barrier of +43.94 eV in the pristine structure to an adsorption well of −0.43 eV in the same nanopore. A negative extremum (a well) indicates that the ion is thermodynamically stabilized within the pore, effectively trapping it. The overall energy profile retains a symmetrical shape with two minima on either side of the graphene. The key modification is the transition from a high central barrier to a deep central well, as shown in Fig. 1.

Ions such as Li^+, Na^+, K^+, Cl^-, and Br^- are examined by studying their penetration through 14-carbon-4 defects in graphene. The results indicate that the 14-carbon-4 defect retains an energy potential barrier, meaning that the ions must overcome this barrier in order to penetrate the graphene sheet from one side to the other. As shown in Fig. 2(a), the penetration process involves first adsorbing on both faces of the graphene sheet before overcoming the potential barrier for full penetration into the graphene sheet. Furthermore, K^+ exhibits the highest energy potential barrier among the tested ions, while Cl^- and Br^- exhibit intermediate potential barriers, with their heights being comparable to those of Na^+. Graphene with 18-carbon-6 defects (six carbon atom vacancies) and the energy wells are −4.73 eV, −4.32 eV, −3.45 eV, −2.08 eV, and −3.02 eV, for Li^+, Na^+, K^+, Cl^-, and Br^-, respectively. For the 18-carbon-6 nanopore structure, the energy barrier between the two potential energy minima vanishes, manifesting as a single minimum potential energy well at the transition state position, as depicted in Fig. 2(b). K^+ shows a small penetration barrier of $\sim$ 0.3 eV, defined as the energy difference from the potential minimum to the central transition state. By increasing the size of defects to 24-carbon-9 and 26-carbon-10, the energy potential barriers of the corresponding ions (Li^+, Na^+, K^+, Cl^-, and Br^-) are eliminated, forming a single potential well as shown in Figs. 2(c) and 2(d).

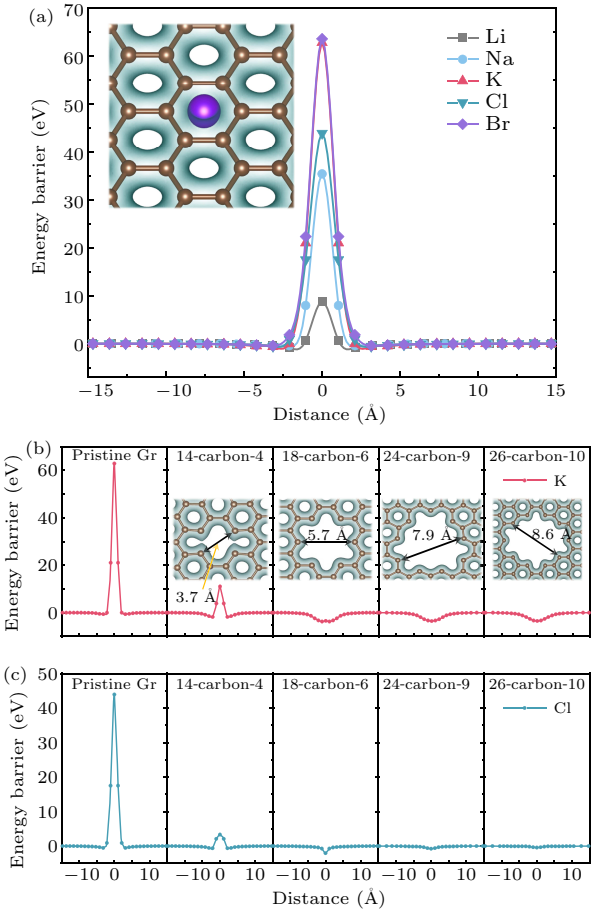


Fig. 1. (a) Reaction energy profiles for ions (Li^+, Na^+, K^+, Cl^-, Br^-) penetrating pristine graphene. Energy profiles for (b) K^+ and (c) Cl^- through graphene nanopore (14-carbon-4, 18-carbon-6, 24-carbon-9, and 26-carbon-10). The insets represent the schematic diagram of a nanochannel. The brown balls represent carbon atoms, and the purple ball represents the penetrating ion.

These defects are shown to diminish both the height and width of the energy barrier that ions must overcome to penetrate the graphene sheet. This combined reduction presents a more accessible pathway for ion traversal. Consequently, the dual lowering of the barrier can be expected to markedly enhance the probability of ion penetration, potentially improving

the efficiency of applications that rely on controlled ion transport, such as ion-selective membranes, sensors, and energy storage devices. The order of energy barrier heights for ion tunneling through 18-carbon-6 defects is $E_{Br} > E_{Cl} > E_K > E_{Na} > E_{Li}$, which is consistent with that of the ionic radius of $R_{Br^-} > R_{Cl^-} > R_{K^+} > R_{Na^+} > R_{Li^+}$, but different from that of the atomic radius of $R_{Br} > R_{Cl} > R_K > R_{Na} > R_{Li}$. Therefore, these species penetrate graphene nanochannels in their ionic form (e.g., Li^+, Na^+, K^+, Cl^-, and Br^-), rather than as neutral atoms.

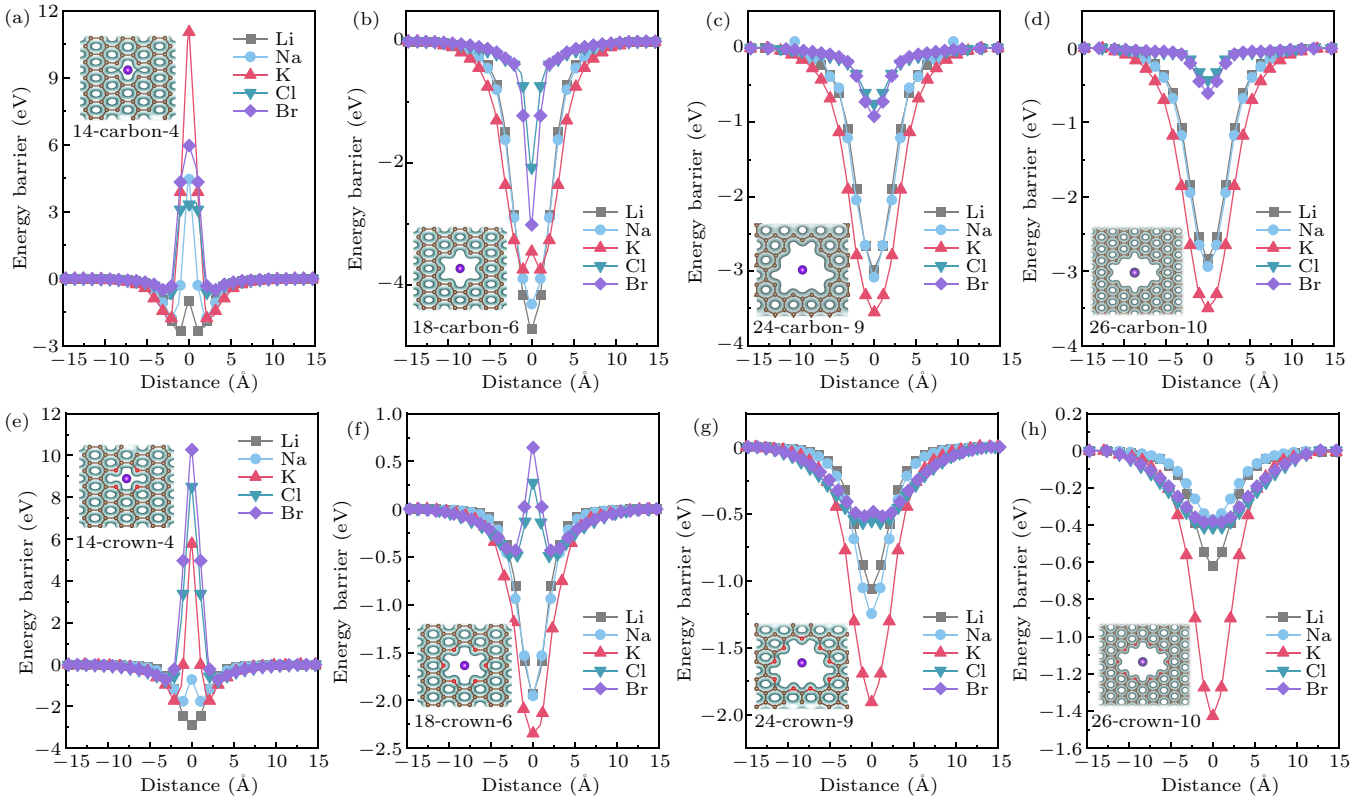


Fig. 2. Reaction energy profiles for direct ion penetration across various types of graphene nanopores. (a)–(d) Pore-defective graphene (14-carbon-4, 18-carbon-6, 24-carbon-9, and 26-carbon-10) and (e)–(h) crown ether-embedded graphene nanopores (14-crown-4, 18-crown-6, 24-crown-9, 26-crown-10). Energy profiles for $Li^+/Na^+/K^+/Cl^-/Br^-$ penetration quantify selective ion permeability. Insets: atomic schematics (gray: C; purple: ions; red/O: crown-ether oxygen).

3.1.3. Charged nanopores

The embedding of crown ether into graphene nanosheets leads to charge transfer between the oxygen atoms at the edges and the nearest neighboring carbon atoms, which in turn imparts a negative charge to the nanopores. This charged nanopore produces functional ion sieving capabilities. In this study, the embedded crown ether structures incorporated into the single-layered graphene nanopores exhibit charged nanoporous characteristics, specifically for the cases of 14-crown-4, 18-crown-6, 24-crown-9, and 26-crown-10. In contrast, the non-incorporated crown ether structures produce non-charged nanoporous characteristics, corresponding to the cases of 14-carbon-4, 18-carbon-6, 24-carbon-9, and 26-carbon-10. These findings are illustrated in Fig. 2. The embedded crown ether structures incorporated into the single-layered graphene nanopores with x-crown-y characteristics also show thermodynamic stability, as shown in Fig. S1 of the supporting information.

Ion transport through the nanopore can be modulated by the charge state of the nanopore. When comparing the charged structures 14-crown-4, 18-crown-6, 24-crown-9, and 26-crown-10 with their uncharged counterparts 14-carbon-4, 18-carbon-6, 24-carbon-9, and 26-carbon-10, variations in the energy profiles for ion penetration are observed. The charged nanopores affect the energy profiles for cation and anion penetration in opposite ways. For structures with a similar defect pore size, the negatively charged structures reduce the penetration energy barrier for cations and increase it for anions, as shown in Figs. 2(e)–2(h) and Table S1 of the supporting information. For instance, in the 14-carbon-4 and 14-crown-4 structures, the energy barriers for Li^+, Na^+, K^+, Cl^-, and Br^- ions are −2.34 eV, 4.45 eV, 11.05 eV, 3.32 eV, and 5.96 eV for the uncharged 14-carbon-4 structure, respectively. In the charged nanopore 14-crown-4 structure, the barriers for Na^+ and K^+ ions diminish to −0.72 eV and 5.77 eV, respectively, while the barriers for chloride and bromine ions increase to 8.50 eV and 10.27 eV, respectively, as shown in Fig. 2 and Table S1 of the supporting information. A similar selective effect is observed for the larger pore. Whereas the neutral 18-carbon-

6 structure presents adsorption wells for all ions, its charged counterpart (18-crown-6) sustains wells for Li^+, Na^+, and K^+ but establishes a pronounced energy barrier against Cl^- and Br^-, as shown in Fig. 2. The specific energy extrema (the central energy maximum or minimum) are listed in Table S1 of the supporting information. These values demonstrate the capability of the charged nanopores to discriminate and sieve anions from cations.

The energy profiles for ion penetration through the nanopores are found to depend on the size of the carbon atom defects in the nanopore. As the pore size increases, the central energy value for ion penetration decreases significantly and can eventually become negative (forming an adsorption well), a trend consistent with that in Subsection 3.1.2. Compared to the energy barriers of pristine graphene (8.81 eV for lithium, 35.45 eV for sodium, 62.87 eV for potassium, 43.94 eV for chlorine, and 63.66 eV for bromine), the charged nanopore 14-crown-4 shows a reduced energy barrier by an order of magnitude, to −2.88 eV, −0.72 eV, 5.77 eV, 8.50 eV, and 10.27 eV, respectively, as shown in Fig. 2(e). For the charged crown-ether nanopores, this enlargement preserves their inherent ability to discriminate between cations and anions, as shown in Figs. 2(f)–2(h).

The selective sieving and separation of anions and cations by graphene nanosheets are determined by the transition state sites. The transition state refers to the position of an ion near the plane of the graphene nanosheet during penetration, as illustrated in the insets of Fig. 3. At the transition state, the ion is situated in the midst of the electron cloud's 'hole'. There is significant electron cloud overlap and transfer between the ion and the carbon atoms of the nanosheet or the oxygen atoms of the crown ether. Comparative analysis of the transition states across various processes *via* differential charge density maps discloses distinct behaviors for cations and anions interacting with nanopores. Cations are consistently observed to lose electrons, as represented by the blue color in Fig. 3. Conversely, anions gain electrons, as indicated by the yellow color. This visualization underscores the differential electronic interactions at the transition state, highlighting the propensity of negatively charged nanopores to interact more favorably with cations. Compared to carbon-defective nanopores alone, the crown ether structure more effectively strips electrons from lithium, sodium, and potassium atoms, while transferring fewer electrons to chlorine and bromine atoms. Consequently, it can be inferred that negatively charged nanopores have a greater affinity for positively charged ions.

Strategically modifying graphene nanosheets with specific defects and charges allows for the fine-tuning of energy profiles, significantly influencing ion sieving and separation. This approach provides a means to enhance the selectivity of graphene membranes for various applications, such as desalination and ion-selective sensing. Understanding the resulting ion transport mechanisms is crucial to advancing graphene-based technologies and developing more efficient, sustainable processes.

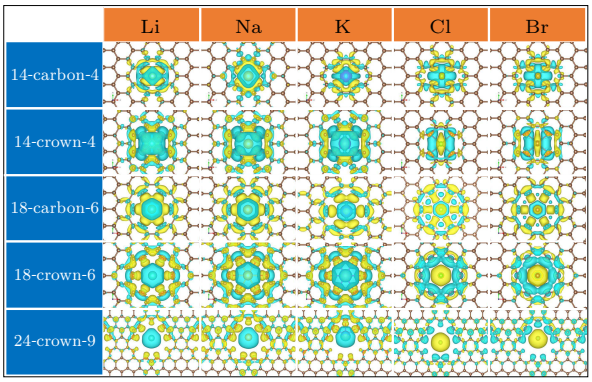


Fig. 3. Charge density difference of the transition states. Transition states of Li^+, Na^+, K^+, Cl^-, and Br^- penetrating the graphene nanopores. The yellow area represents an increase in electron density, while the blue area represents a decrease in electron density.

3.2. Charge selectivity

3.2.1. Diffusion selectivity

The ion transport behavior is investigated in a concentration gradient-driven system utilizing crown ether-embedded graphene nanopores, as shown in Fig. 4(a). A freestanding graphene membrane, functionalized with crown ether moieties within its nanopores, partitions two isolated chambers containing KCl solutions of differing concentrations (left chamber: 0.5 mol·L^{-1}, right chamber: 0 mol·L^{-1}).

The selection of K^+ and Cl^- was primarily driven by their unique ability to simultaneously resolve the interplay between steric confinement and electrostatic repulsion within a single simulation — this offers the most direct mechanistic validation. Additionally, KCl serves as a canonical experimental benchmark, ensuring the results are broadly comparable and facilitating future validation.

Ionic exchange occurs exclusively through these functionalized nanopores, driven solely by the chemical potential difference across the membrane. The measurements focus on the resultant ionic flux through the nanopores under this concentration bias. All three crown ether-modified nanopore structures ("24-crown-9", "26-crown-10", "30-crown-12") exhibit a consistent cation-selective permeation trend: positively charged K^+ ions permeate more readily than negatively charged Cl^- ions through the negatively charged nanopores, as shown in Figs. 4(b)–4(d). This observation confirms that crown ether produces a negative charge along the pore periphery, enabling effective charge-based ion sieving. Consequently, negatively charged nanopores preferentially facilitate the translocation of counter-ions (cations) while impeding the passage of co-ions (anions).

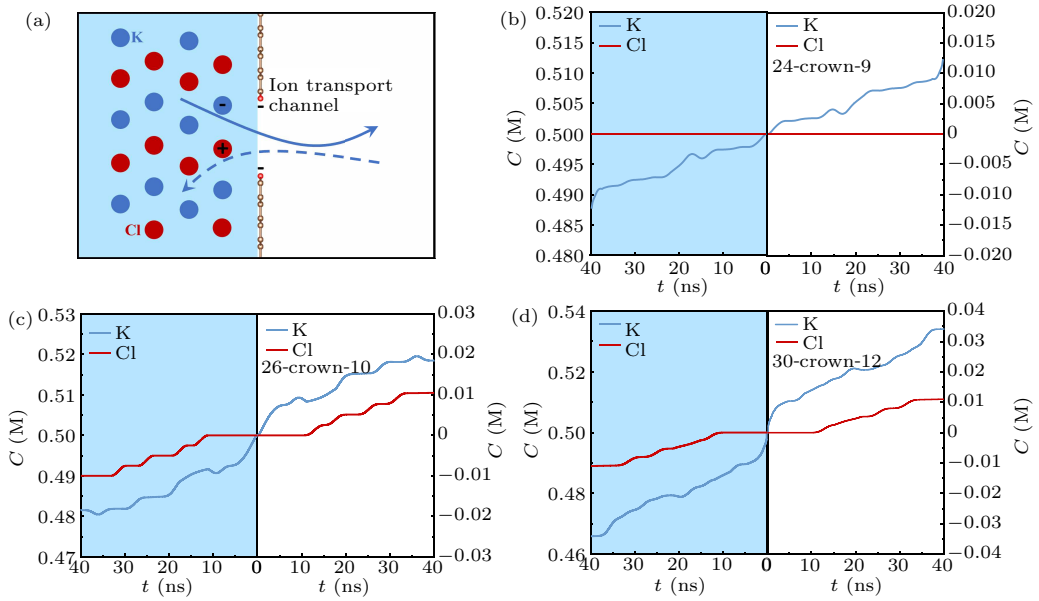


Fig. 4. (a) Ions diffusion simulation system: time-dependent distribution of KCl concentrations in left and right reservoirs under $C_l \gg C_r$ condition, separated by crown ether-embedded graphene membranes with ion-transporting nanopores. (b) 24-crown-9 membrane, (c) 26-crown-10 membrane, (d) 30-crown-12 membrane. Note: Left graph portions represent left reservoirs; right portions represent right reservoirs.

Furthermore, the study reveals a significant dependence of ion selectivity on nanopore diameter. Among the three crown ether structures evaluated, the nanopore with the smallest aperture ("24-crown-9") exhibits the most pronounced cation permselectivity. This structure effectively blocks anion translocation while maintaining enhanced K^+ permeability. This finding underscores that the effectiveness of charge-selective sieving in crown ether-embedded graphene nanopores is critically modulated by the physical confinement imposed by the pore size, as shown in Fig. 4(b). Smaller nanopores impose stricter steric and electrostatic constraints, leading to significantly heightened selectivity favoring cations over anions during free diffusion under a concentration gradient. The results demonstrate the intrinsic cation selectivity arising from the negative charge introduced by crown ethers in graphene nanopores and highlight the pore size as a key parameter to optimize selective ion transport in these nanoconfined environments driven by osmotic forces.

3.2.2. Electroosmotic flow

Based on the discussion of the energy profiles for ion penetration through crown ether-modified nanopores, modifications of size and charge alter the energy barriers/wells for anion and cation penetration. It is thus predicted that the crown ether structure can sieve and separate anions and cations. For validation, the nanopore structure after crown ether modification is immersed in a KCl aqueous solution, and its ion charge sieving and separation capabilities are studied under the influence of an external electric field, as shown in Fig. 5(a). When a bias is applied along the z-axis, potassium (K^+) and chloride (Cl^-) ions undergo directed migration under the influence of the electric field, which in turn generates an ionic current (I). The ionic current is expressed by the following formula:

$$I = \sum_i q_i v_i / H, \tag{2}$$

where H denotes the height of the simulated system, while q_i and v_i represent the charge and velocity of the i-th ion, respectively. The total charge passing through the nanopores is defined by the integral

$$Q = \int I_t \, \mathrm{d}t. \tag{3}$$

The ionic current I and the total ionic charge Q offer direct insights into the dynamics of ion penetration within the nanopores.

When a positive or negative bias is applied perpendicular to the direction of the nanosheet, a distinct ionic current is observed to be generated. The application of external biases of $E = 0.010$ V/Å and $E = 0.005$ V/Å results in the vertical traversal of charge carriers through the graphene nanosheet, with the current magnitude depending on the external bias. A potential with equal magnitude but opposite direction results in equal and oppositely directed ion currents, as shown in Fig. 5(b). This graphene nano-ionic channel embedded with crown ether is symmetrical on both sides of the nanosheet, as corroborated by the energy profiles. When no external bias is applied, no ionic current through the nanopores is detected. The measured ionic current is a combined effect of potassium (K^+) and chloride (Cl^-) ion flows. At a fixed electric field, K^+ and Cl^- ions move in opposite directions. Consequently, at zero external bias, neither potassium nor chloride ions exhibit the penetration behavior. Subsequently, the individual contributions of potassium and chloride ion currents through the negatively charged crown ether nanopores are analyzed. Potassium ions generate a significant ionic current,

whereas chloride ions do not produce a current, as shown in Fig. 5(c). Considering that the transport process in the symmetrical nano-ionic pore channel does not have a directional bias, the conclusion of potassium and chloride ions under negative bias is consistent with that at a positive bias. All in all, the crown ether-embedded graphene with negatively charged nanopores exhibits preferential permeation for potassium ions while impeding the passage of chloride ions.

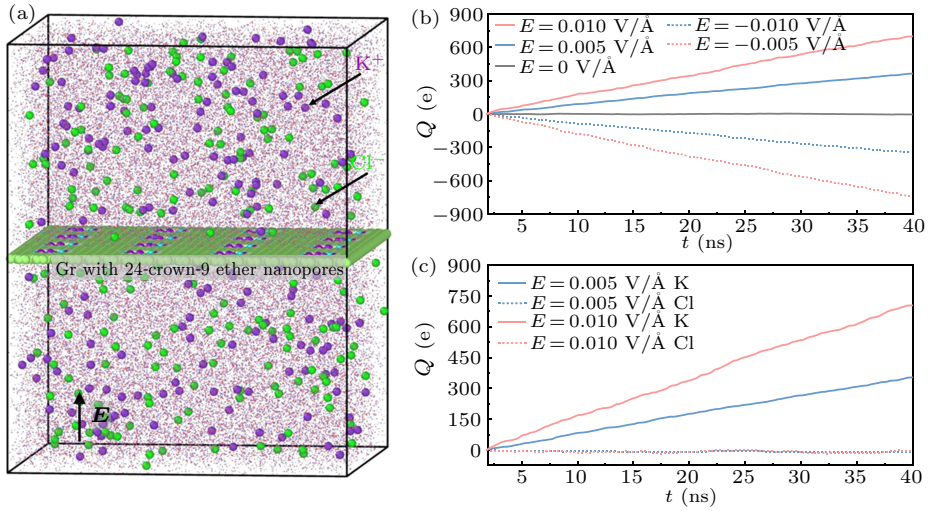


Fig. 5. Ionic transport dynamics under an electroosmotic flow field. (a) Electroosmotic flow simulation system: atoms and ions are represented as van der Waals spheres, and water molecules are displayed transparently. Ionic currents through nanopores in single-layer graphene with a defect (24-crown-9) in 0.5-mol/L KCl solution. (b) Total charges of ions moving through the nanopore *versus* time t, at various applied biasing voltages. (c) Detailed breakdown of the individual ionic currents for K^+ and Cl^-.

3.3. Selectivity mechanism

To elucidate the screening mechanism of charged nanopores for anions and cations, it is necessary to consider both the energy profiles for ion penetration through graphene nanosheets and the behavior of ions in aqueous solutions. The energy barrier at the mouth of the nanochannel is an important intrinsic factor affecting the ionic conductivity in two-dimensional, sub-nanometer-scale channels. Based on the discussions in Subsection 3.1, there are energy barriers as well as energy wells for ion penetration through graphene nanopores. Combining the solution to the tunneling probability formula through a one-dimensional potential barrier

$$p = \exp\left[\frac{-2x\sqrt{2m(V-E)}}{\hbar}\right]. \tag{4}$$

Ion tunneling through nanopores is closely related to the heights of the energy barriers and wells. Generally, the lower the barrier height or the shallower the well depth, the easier it is for a single ion to penetrate the graphene nanopore. However, in a mixed aqueous solution of anions and cations, the penetration process is also influenced by the environment in which the ions are situated.

For nanopores with small diameters, such as 14-carbon-4 and 14-crown-4, there are high tunneling barriers for potassium and chloride ions ranging from 3 eV to 11 eV. At room temperature, the average translational kinetic energy of ions is $3kT/2$ (~ 0.03 eV), which is insufficient to penetrate such nanopores. For the 24-crown-9 graphene nanopores, both potassium and chloride ions encounter energy wells, with the well for bromide ions being shallower. Considering the perspective of a single particle penetrating the energy profiles, the 24-crown-9 nanopore is more likely to allow penetration of chloride ions than potassium ions. This is in contrast to the results derived by molecular dynamics simulations. Despite quantitative differences arising from the distinct physical premises (vacuum *versus* solvated environment, 0 K *versus* room temperature), the NEB-derived relative stability ordering ($K^+ > Cl^-$) remains qualitatively consistent with the solution-phase free energy profile, as shown in Fig. S2 of the supporting information. This consistency supports the use of the NEB-derived ordering as a meaningful indicator for predicting selective ion enrichment under solution conditions. Accordingly, the deeper well for K^+ leads to its preferential capture and intra-pore pre-concentration, whereas Cl^-, lacking such a well, remains depleted. This pre-concentrated reservoir of K^+ then becomes the prerequisite for sustained cation conduction under an applied electric field, as directly observed in the MD simulations.

To elucidate the physical mechanisms governing selective anion/cation screening by charged nanopores, the two-dimensional lateral density distributions of ions within the graphene nanochannels are analyzed. Specifically, the in-plane (XY-plane) ion concentrations across the graphene nanosheet plane (integrated over $z = 49$–52 Å, centered at the nanopore location $z_0 = 50.5$ Å) are quantified.[35,36] The critical function of the adsorption well is revealed here: it leads to the intra-pore enrichment of charge carriers. In the absence of an external electric field ($E = 0$ V/Å), the nega-

tively charged crown-ether nanopores capture and concentrate a significant amount of K^+ ions within the pore, while Cl^- ions remain depleted, as shown in Figs. 6(a) and 6(d). This is the direct consequence of the energy landscape: the well for K^+ enables its thermodynamic stabilization, whereas the barrier for Cl^- prevents its accumulation. As an external field is applied, the pre-concentrated K^+ ions are drawn through the pore, sustaining a cation current. The local K^+ concentration decreases with increasing field as ions are flushed out, as shown in Figs. 6(a)–6(c), demonstrating a dynamic cycle of capture and conduction. In stark contrast, Cl^- ions remain depleted at all field strengths, as shown in Figs. 6(d)–6(f), as they lack an initial intra-pore reservoir due to the repulsive barrier. Therefore, the selectivity arises not merely from differing penetration barriers, but from the asymmetric ability of the pore to pre-concentrate cations versus anions, which dictates the availability of charge carriers for subsequent field-driven transport.

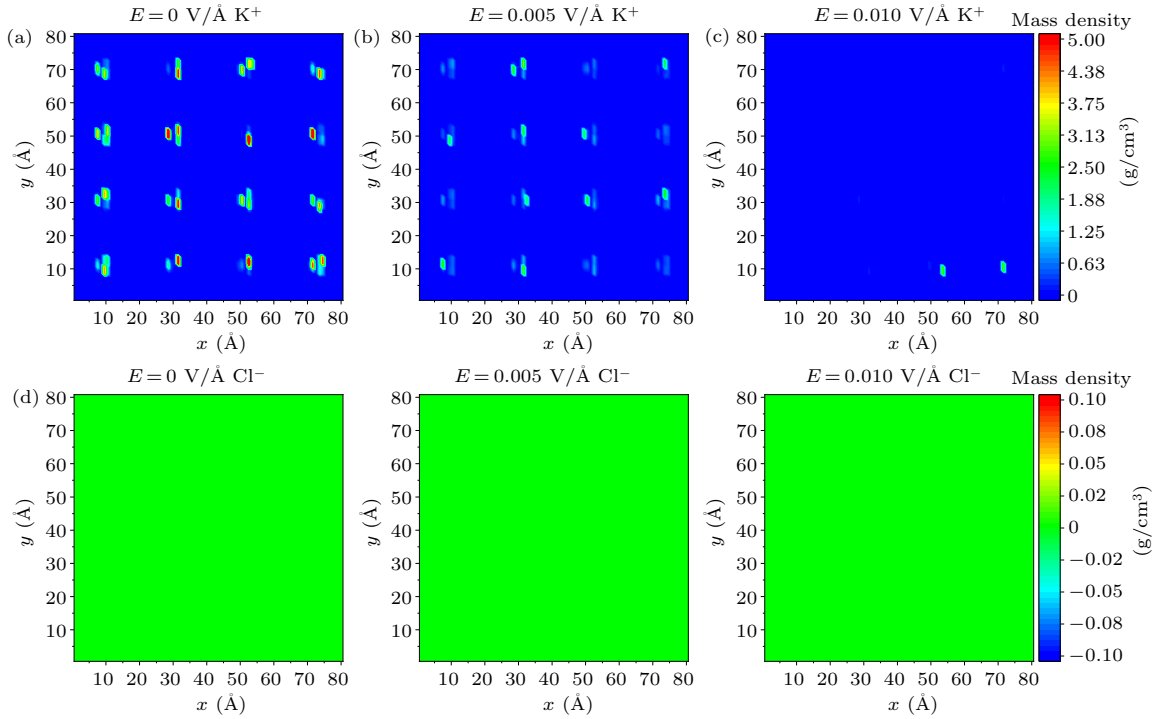


Fig. 6. Lateral (XY-plane) mass density distributions of K^+ and Cl^- in the 24-crown-9 system, integrated across the graphene nanosheet plane ($z = 49.0$ Å–52.0 Å; graphene centered at $z = 50.5$ Å). (a)–(c) K^+ distributions under biases of (a) 0 V/Å, (b) 0.005 V/Å, and (c) 0.010 V/Å. (d)–(f) Corresponding Cl^- distributions under (d) 0 V/Å, (e) 0.005 V/Å, and (f) 0.010 V/Å.

4. Conclusion

Atomic-scale defect engineering enables the construction of graphene nanochannels with tailored crown-ether pores, achieving programmable ion selectivity through pore geometry and charge modulation. The 24-crown-9 functionalized architecture exhibits exceptional cation selectivity, generating cationic current exceeding anionic current by 100-fold *via* the steric-electrostatic synergy. Mechanistic analysis reveals that negatively charged defects reduce the free energy barriers for cations (e.g., Li^+, Na^+, K^+) while elevating barriers for anions (e.g., Cl^-, Br^-), while ion transport is governed by electroosmotic dynamics. These findings establish a design framework for biomimetic ion-exchange membranes, advancing applications in nanofluidic circuits and energy-efficient separation technologies.

Acknowledgements

Project supported by the National Natural Science Foundation of China (Grant Nos. 52473251 and 52403315), the Industry University Research Cooperation Fund of the Eighth Research Institute of China Aerospace Science and Technology Corporation (Grant No.SAST2023-030), the National Key Research and Development Program of China (Grant No. 2021YFB3900701), Scientific and Technologial Innovation Program of Higher Education Institutions in Shanxi Province, China (Grant No. 2025L142), and City University of Hong Kong Donation Research Grant (Grant Nos. DONRMG 9229021 and 9220061).

References

[1] Deursen P M G, Tang Z, Winter A, Mohn M J, Kaiser U, Turchanin A A and Schneider G F 2019 *Nanoscale* **11** 20785
[2] Walker M I, Ubych K, Saraswat V, Chalklen E A, Braeuninger-Weimer P, Caneva S, Weatherup R S, Hofmann S and Keyser U F 2017 *ACS Nano* **11** 1340
[3] Esfandiar A, Radha B, Wang F C, Yang Q, Hu S, Garaj S, Nair R R, Geim A K and Gopinadhan K 2017 *Science* **358** 511
[4] Xiao K, Li D J and Wu C X 2018 *Chin. Phys. B* **27** 024702
[5] Sahu S and Zwolak M 2019 *Rev. Mod. Phys.* **91** 21004
[6] Aluru N R, Aydin F, Bazant M Z, Blankschtein D, Brozena A H, de Souza J P, Elimelech M, Faucher S, Fourkas J T, Koman V B, Kuehne

M, Kulik H J, Li H K, Li Y, Li Z, Majumdar A, Martis J, Misra R P, Noy A, Pham T A, Qu H, Rayabharam A, Reed M A, Ritt C L, Schwegler E, Siwy Z, Strano M S, Wang Y, Yao Y C, Zhan C and Zhang Z 2023 *Chem. Rev.* **123** 2737
[7] Bhardwaj A, Surmani Martins M V, You Y, Sajja R, Rimmer M, Goutham S, Qi R, Abbas Dar S, Radha B and Keerthi A 2024 *Nat. Protoc.* **19** 240
[8] Kim S, Choi H, Kim B, Lim G, Kim T, Lee M, Ra H, Yeom J, Kim M, Kim E, Hwang J, Lee J S and Shim W 2023. *Adv. Mater.* **35** 2206354
[9] Zhang X Q, Wen L P and Jiang L 2019 *Acta Phys. Sin.* **68** 018801 (in Chinese)
[10] Abdulazeez I 2022 *J. Phys. Chem. Solids* **171** 110983
[11] Kochaev A, Katin K and Maslov M 2023 *Mater. Today Chem.* **30** 101512
[12] Xin Y, Gao Q, Huang J, Gao J, Geng X, Shi H, Wang M, Xiao Z, Chu P K and Huang A 2023 *Mater. Today Chem.* **34** 101767
[13] Fang A, Kroenlein K, Riccardi D and Smolyanitsky A 2019 *Nat. Mater.* **18** 76
[14] Noh Y and Smolyanitsky A 2024 *J. Phys. Chem. Lett.* **15** 665
[15] Smolyanitsky A, Paulechka E and Kroenlein K 2018 *ACS Nano* **12** 6677
[16] Ge M, Wei C, Fang T and Liu X 2024 *Sep. Purif. Technol.* **338** 126415
[17] Bang K R, Bahamon D, Vega L F and Cho E S 2020 *Adv. Mater. Interfaces* **7** 1901876
[18] Ye Y S, Mohamed M G, Tsai M C, Hu H Y, Hwang B J and Kuo S W 2024 *J. Mater. Chem. A* **12** 25346
[19] Baudino L, Pedico A, Bianco S, Periolatto M, Pirri C F and Lamberti A 2022 *Membranes* **12** 233
[20] Jing Z, Wang G, Zhou Y, Pang D, Zhu F and Liu H 2020 *J. Mol. Liq.* **311** 113305
[21] Zhang Y, Di F, Li P and Xiong R 2022 *Chem. Eur. J.* **28** e202102990
[22] Li J, Yim D, Jang W D and Yoon J 2017 *Chem. Soc. Rev.* **46** 2437
[23] Kresse G and Furthmüller J 1996 *Phys. Rev. B* **54** 11169
[24] Perdew J P, Burke K and Ernzerhof M 1996 *Phys. Rev. Lett.* **77** 3865
[25] Sheppard D, Xiao P, Chemelewski W, Johnson D D and Henkelman G 2012 *J. Chem. Phys.* **136** 074103
[26] Trucano P and Chen R 1975 *Nature* **258** 136
[27] Momma K and Izumi F 2011 *J. Appl. Crystallogr.* **44** 1272
[28] Thompson A P, Aktulga H M, Berger R, Bolintineanu D S, Brown W M, Crozier P S, Pieter J, Kohlmeyer A, Moore S G, Dac T, Shan R, Stevens M J, Tranchida J, Trott C and Plimpton S J 2022 *Comput. Phys. Commun.* **271** 108171
[29] Miao M, Nardelli M B, Wang Q and Liu Y 2013 *Phys. Chem. Chem. Phys.* **15** 16132
[30] Xin Y, Huang A, Hu Q, Shi H, Wang M, Xiao Z, Zheng X, Di Z and Chu P K 2018 *Adv. Theory Simul.* **1** 1700009
[31] Hu S, Lozada-Hidalgo M, Wang F C, Mishchenko A, Schedin F, Nair R R, Hill E W, Boukhvalov D W, Katsnelson M I, Dryfe R A W, Grigorieva I V, Wu H A and Geim A K 2014 *Nature* **516** 227
[32] Lin A, Shi J, Wei S H and Sun Y Y 2024 *Chin Phys. B* **33** 086601
[33] Han M X, Ji Z Y, Shang L W, Chen Y P, Wang H, Liu X, Li D M and Liu M 2011 *Chin Phys. B* **20** 086102
[34] Xu W Y, Huang L, Que Y D, Lin X, Wang Y L, Du S X and Gao H J 2014 *Chin Phys. B* **23** 088108
[35] Wang Y, Kiziltas A, Blanchard P and Walsh T R 2021 *Comput. Phys. Commun.* **266** 108032
[36] Humphrey W, Dalke A and Schulten K 1996 *J. Mol. Graph.* **14** 33